Structural Eng./Earthquake Eng., JSCE, Vol. 13, No. 2, 175s—185s, 1996 October

ELASTIC ANALYSIS OF AXI-SYMMETRIC FINITE CYLINDER CONSTRAINED RADIAL DISPLACEMENT ON THE LOADING END

Shouhei WATANABE[1]

[1] Member of JSCE, Dr. Agr. Associate Professor, Faculty of Agr., Tottori University
(Koyama, Tottori 680, JAPAN)

In the usual compression test of a cylinder, there exists friction on the loading end. Accordingly, radial displacement on the end will be constrained to some extent. An elastic analysis of such axi-symmetric cylinders is presented in this paper using stress function with infinite series. Distribution of radial displacement on the end was given by the Fourier-Bessel expansion. Numerical results were obtained for some combinations of size ratio, confining pressure and degree of constraint. Distributions of stresses, strains and displacements in the cylinder were investigated for several cases, and were compared with the results obtained with the finite element method.

Key Words : *elastic, finite cylinder, constrained end, stress function, infinite series, Fourier-Bessel expansion, finite element method*

1. INTRODUCTION

Filon[1)] has presented elastic analyses of finite cylinders subjected to axi-symmetric axial loads. He has given solutions for the isotropic homogeneous elastic cylinders under the conditions of perfectly constrained radial displacement on the whole face or only the perimeter of the loading end. Kimura[2)] has supplementarily examined Filon's analyses, and has carried out unconfined compression tests using mortar cylinders. In these tests, he also clamped the perimeter of the loading end with an iron hoop in order to relate the experimental condition with the analytical condition. However, in the usual compression test, free radial displacement on the loading end will be partially constrained according to the friction between the platen and cylinder. The stresses, strains and displacements in the cylinder are considered to differ from those of the frictionless condition. Therefore, a number of tests and analyses have been carried out by many investigators changing the conditions of the loading end and size ratio.

Saito[3)] has presented elastic analyses of cylinders subjected to axi-symmetric loads on part of the loading end and the side surface. Yamaguchi[4)] has summarized this method, while Ogaki *et al.*[5)] has analyzed one of these using a different method. The present paper deals with the problems encountered in the usual unconfined or confined compression tests. Namely, when a cylinder is subjected to an unconfined or confined axial symmetrical load, the loading end of the cylinder displaces toward the axial direction retaining a flat plane, but a part of the free radial displacement on the loading end will be constrained by the friction between the platen and the cylinder. An elastic analytical solution for this cylinder is derived in this paper. This problem has a displacement boundary condition on the loading end and a stress boundary condition on the side surface. An equilibrium equation is also needed. Furthermore, comparisons of the distribution of the side surface displacement and the contours of stresses and strains between frictionless and constrained conditions were made using the numerical results of the analytical solutions. The numerical computations were carried out under several cases of size ratio, degree of constraint, pressure ratio and radial displacement form.

The solution obtained in this paper can be computed by the finite element method, but the results obtained for the axial symmetrical problem are dependent on the mesh and on the method of treating the [B] matrix. Analytical solutions were useful to estimate the accuracy of the results obtained with the finite element method. Moreover, analytical solutions have the advantage of providing precise results of stresses, strains and displacements at any point in a cylin-

This paper is translated into English from the Japanese paper, which originally appeared on *J. Struct. Mech. Earthquake Eng., JSCE*, No.450/I-20, pp.85-94, 1992.7.

der. In addition, in the finite element method one cannot give force and displacement simultaneously at one point as a boundary condition. Accordingly, when force or displacement are given as boundary conditions, the results of the finite element method should be revised. The effects of the revision method and mesh on the accuracy of the finite element method are discussed in this paper.

There exist various theories for the mechanics of fracture concerning unconfined or confined compression tests of concrete and mortar cylinders. Various tests and both elastic and elastoplastic analyses have been carried out to verify the fracture theories. Elastic analyses cannot perfectly describe the fracture mechanism. However, it is considered that elastic analyses are a basic requirement for this problem.

2. PROBLEMS AND BASIC SOLUTIONS

As illustrated in **Fig. 1(a)**, we will assume an isotropic homogeneous finite cylinder of radius a and height $2h$ subjected to uniform loads q_0 on the ends and confining pressure p_0 on the side with no friction on both surfaces. The loading end will displace uniformly toward the z direction and the side surface will displace uniformly toward the r direction like the broken lines shown in **Fig. 1(a)**. The stresses and strains in the cylinder are uniform[6] and are described by the following equations:

$$\left.\begin{aligned} &\sigma_z = q_0,\ \ \sigma_r = \sigma_t = p_0,\ \ \tau_{rz} = \gamma_{rz} = 0 \\ &\epsilon_z = (-2\nu p_0/q_0 + 1)q_0/E \\ &\epsilon_r = \epsilon_t = \{(1-\nu)p_0/q_0 - \nu\}q_0/E \\ &w_0 = (-2\nu p_0/q_0 + 1)q_0 h/E \\ &u_0 = \{(1-\nu)p_0/q_0 - \nu\}q_0 a/E \end{aligned}\right\} \quad (1)$$

in which, E =Young's modulus, ν=Poisson's ratio, and $\sigma_z, \sigma_r, \sigma_t$ are normal stresses in the axial, radial and circumferential directions respectively, τ_{rz} is the shearing stress in the rz plane, and $\epsilon_z, \epsilon_r, \epsilon_t$ and γ_{rz} are the strains corresponding to those stresses. In addition, w_0 and u_0 are the axial displacement of the loading end and the radial displacement of the side surface respectively. These stresses, strains and displacements are defined as basic solutions in this paper. When we use dimensionless distances ρ and η by $\rho = r/a$ and $\eta = z/h$, displacements of any point of the cylinder toward the radial and axial directions can be described as $u = u_0\rho$ and $w = w_0\eta$ respectively.

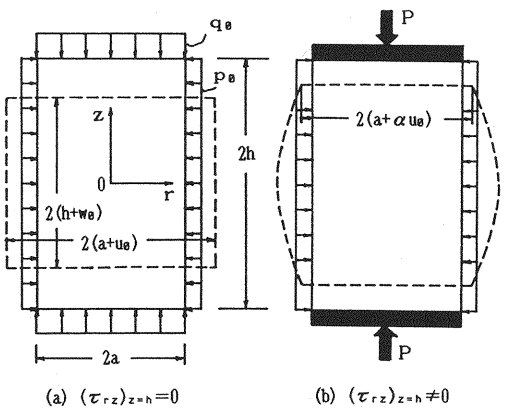

Fig.1 Definition and typical deformation of cylinders induced by compression tests.

However, friction exists between the platen and cylinder in the usual compression tests. In this case, the loading ends are kept flat but free radial displacement will be somewhat constrained. As a result, the uniformity of stresses and strains in the cylinder will decay, and the side surface will deform as illustrated in **Fig. 1(b)**. The factor α shown in **Fig. 1(b)** indicates the reduction coefficient of u_0 or the degree of constraint of free radial displacement on the loading end. This means that $\alpha = 0$ when the radial displacements on the ends are perfectly constrained, and $\alpha = 1$ represents the frictionless condition. In the usual compression tests, the value of α lies between them, while the distribution of load intensity and axial displacement on the loading end are unknown. However, the relation between mean load intensity q_0 and total load P can be written as

$$P = \pi a^2 q_0 \quad (2)$$

Stresses, strains and displacements will no longer be uniform in this case, and these distributions will differ from the basic ones. The main objective of this paper is to obtain an elastic solution of this case. Loads and displacements have a positive or negative sign in **Fig.1**. If we define tension as positive, P, q_0, p_0, w_0 are negative and u_0 is positive.

3. METHOD OF ANALYSIS

(1) Boundary conditions and equilibrium equation

We assume that the flat platens in **Fig.1(b)** displace parallel to the abscissa. The boundary conditions and the equilibrium equations of this cylinder are

$$\text{on } r=a, \qquad \sigma_r = p_0 \tag{3a}$$

$$\text{on } r=a, \qquad \tau_{rz} = 0 \tag{3b}$$

$$\text{on } z \pm h, \qquad \frac{\partial w}{\partial r} = 0 \tag{3c}$$

$$\text{on } z \pm h, \qquad u = f(r) \tag{3d}$$

$$\text{on each } z, \qquad \int_0^a \sigma_z 2\pi r dr = P \tag{3e}$$

(2) Analyses by stress function

Stresses and displacements for the axisymmetric problem have been expressed by a function ϕ[7)]

$$\left.\begin{aligned}
\sigma_z &= \frac{\partial}{\partial z}\left\{(2-\nu)\nabla^2\phi - \frac{\partial^2\phi}{\partial z^2}\right\} \\
\sigma_r &= \frac{\partial}{\partial z}\left(\nu\nabla^2\phi - \frac{\partial^2\phi}{\partial r^2}\right) \\
\sigma_t &= \frac{\partial}{\partial z}\left(\nu\nabla^2\phi - \frac{1}{r}\cdot\frac{\partial\phi}{\partial r}\right) \\
\tau_{rz} &= \frac{\partial}{\partial r}\left\{(1-\nu)\nabla^2\phi - \frac{\partial^2\phi}{\partial z^2}\right\} \\
\frac{wE}{1+\nu} &= \left\{2(1-\nu)\nabla^2\phi - \frac{\partial^2\phi}{\partial z^2}\right\} \\
\frac{uE}{1+\nu} &= -\frac{\partial^2\phi}{\partial r\partial z}
\end{aligned}\right\} \tag{4}$$

in which,

$$\nabla^2 = \frac{\partial^2}{\partial r^2} + \frac{1}{r}\cdot\frac{\partial}{\partial r} + \frac{\partial^2}{\partial z^2} \tag{5}$$

and ϕ is the function which satisfies the following equation.

$$\nabla^2\nabla^2\phi = 0 \tag{6}$$

If the cylinder is subjected to symmetric loads as shown in **Fig. 1**, $\sigma_z, \sigma_r, \sigma_t$ and u are even functions with respect to z axis, and τ_{rz} and w are odd functions. Now, we define the size ratio as $\kappa = h/a$, and we shall use a stress function ϕ given in the following equation:

$$\begin{aligned}
\phi = q_0 a^3 \Bigg[& A_0\frac{\kappa^3\eta^3}{6} + C_0\frac{\kappa\eta\rho^2}{2} \\
& + \sum_{n=1}^{\infty}\frac{\sin(n\pi\eta)}{{\beta_n}^3}\{A_n I_0(\beta_n\rho) + B_n\beta_n\rho I_1(\beta_n\rho)\} \\
& + \sum_{s=1}^{\infty}\frac{J_0(\lambda_s\rho)}{{\lambda_s}^3}\{C_s\sinh\gamma_s\eta + D_s\gamma_s\eta\cosh\gamma_s\eta\}\Bigg]
\end{aligned} \tag{7}$$

in which, λ_s is the s-th zero of $J_1(x)$, $\beta_n = n\pi/\kappa$, $\gamma_s = \lambda_s\kappa$, and $A_0, C_0, A_n, B_n, C_s, D_s$ are coefficients determined from the boundary conditions.

Substituting Eq. (7) into Eq. (4), we obtain

$$\begin{aligned}
\tau_{rz}/q_0 = & \sum_{n=1}^{\infty}\sin(n\pi\eta)[A_n I_1(\beta_n\rho) \\
& + B_n\{(2-2\nu)I_1(\beta_n\rho) + \beta_n\rho I_0(\beta_n\rho)\}] \\
& + \sum_{s=1}^{\infty} J_1(\lambda_s\rho)\{C_s\sinh\gamma_s\eta \\
& + D_s(2\nu\sinh\gamma_s\eta + \gamma_s\eta\cosh\gamma_s\eta)\} \\
\frac{wE}{1+\nu}/(q_0 a) = & \{A_0(1-2\nu) + C_0(4-4\nu)\}\kappa\eta \\
& + \sum_{n=1}^{\infty}\frac{\sin(n\pi\eta)}{\beta_n}[A_n I_0(\beta_n\rho) \\
& + B_n\{(4-4\nu)I_0(\beta_n\rho) + \beta_n\rho I_1(\beta_n\rho)\}] \\
& + \sum_{s=1}^{\infty}\frac{J_0(\lambda_s\rho)}{\lambda_s}[-C_s\sinh\gamma_s\eta \\
& + D_s\{(2-4\nu)\sinh\gamma_s\eta - \gamma_s\eta\cosh\gamma_s\eta\}]
\end{aligned} \tag{8}$$

We obtain the following equations from Eqs. (8),(3a),(3c)

$$\left.\begin{aligned}
\frac{A_n I_1}{2-2\nu+\beta_n I_0/I_1} &= \frac{B_n I_1}{-1} = G_n \\
\frac{C_s\sinh\gamma_s}{2-4\nu-\gamma_s\coth\gamma_s} &= \frac{D_s\sinh\gamma_s}{1} = H_s
\end{aligned}\right\} \tag{9}$$

in which, $I_0 = I_0(\beta_n)$, $I_1 = I_1(\beta_n)$, and G_n, H_s are unknown coefficients which replace A_n, B_n, C_s, D_s. Considering Eq. (9) and substituting Eq. (7) into Eq. (4), we obtain the following equations for stresses and displacements.

$$\begin{aligned}
\sigma_z/q_0 = & A_0(1-\nu) + C_0(4-2\nu) \\
& + \sum_{n=1}^{\infty} G_n\cos(n\pi\eta)\left\{\left(-2+\beta_n\frac{I_0}{I_1}\right)\frac{I_0(\beta_n\rho)}{I_1} \right. \\
& \qquad \left. - \beta_n\rho\frac{I_1(\beta_n\rho)}{I_1}\right\} \\
& + \sum_{s=1}^{\infty} H_s J_0(\lambda_s\rho)\left\{(-1+2\nu+\gamma_s\coth\gamma_s) \right. \\
& \qquad \left. \times\frac{\cosh\gamma_s\eta}{\sinh\gamma_s} - \gamma_s\eta\frac{\sinh\gamma_s\eta}{\sinh\gamma_s}\right\} \\
\sigma_r/q_0 = & A_0\nu + C_0(2\nu-1) \\
& + \sum_{n=1}^{\infty} G_n\cos(n\pi\eta)\left\{\left(-1-\beta_n\frac{I_0}{I_1}\right)\frac{I_0(\beta_n\rho)}{I_1} \right. \\
& \qquad + \beta_n\rho\frac{I_1(\beta_n\rho)}{I_1} \\
& \qquad \left. + \left(2-2\nu+\beta_n\frac{I_0}{I_1}\right)\frac{I_1(\beta_n\rho)}{I_1}\cdot\frac{1}{\beta_n\rho}\right\} \\
& + \sum_{s=1}^{\infty} H_s\Bigg[J_0(\lambda_s\rho)\Big\{(3-2\nu-\gamma_s\coth\gamma_s)
\end{aligned}$$

$$\times \frac{\cosh\gamma_s\eta}{\sinh\gamma_s} + \gamma_s\eta\frac{\sinh\gamma_s\eta}{\sinh\gamma_s}\Big\}$$
$$+ \frac{J_1(\lambda_s\rho)}{\lambda_s\rho}\Big\{(-3+4\nu+\gamma_s\coth\gamma_s)$$
$$\times \frac{\cosh\gamma_s\eta}{\sinh\gamma_s} - \gamma_s\eta\frac{\sinh\gamma_s\eta}{\sinh\gamma_s}\Big\}\Big]$$

$$\sigma_t/q_0 = A_0\nu + C_0(2\nu-1)$$
$$+ \sum_{n=1}^{\infty} G_n\cos(n\pi\eta)\Big\{(1-2\nu)\frac{I_0(\beta_n\rho)}{I_1}$$
$$+ \Big(-2+2\nu-\beta_n\frac{I_0}{I_1}\Big)\frac{I_1(\beta_n\rho)}{I_1}\cdot\frac{1}{\beta_n\rho}\Big\}$$
$$+ \sum_{s=1}^{\infty} H_s\Big[J_0(\lambda_s\rho)\Big(2\nu\frac{\cosh\gamma_s\eta}{\sinh\gamma_s}\Big)$$
$$+ \frac{J_1(\lambda_s\rho)}{\lambda_s\rho}\Big\{(3-4\nu-\gamma_s\coth\gamma_s)$$
$$\times \frac{\cosh\gamma_s\eta}{\sinh\gamma_s} + \gamma_s\eta\frac{\sinh\gamma_s\eta}{\sinh\gamma_s}\Big\}\Big]$$

$$\tau_{rz}/q_0 = \sum_{n=1}^{\infty} G_n\sin(n\pi\eta)\Big(\beta_n\frac{I_0}{I_1}\cdot\frac{I_1(\beta_n\rho)}{I_1}$$
$$- \beta_n\rho\frac{I_0(\beta_n\rho)}{I_1}\Big)$$
$$+ \sum_{s=1}^{\infty} H_s J_1(\lambda_s\rho)\Big\{(2-2\nu-\gamma_s\coth\gamma_s)$$
$$\times \frac{\sinh\gamma_s\eta}{\sinh\gamma_s} + \gamma_s\eta\frac{\cosh\gamma_s\eta}{\sinh\gamma_s}\Big\}$$

$$\frac{wE}{1+\nu}/(q_0a) = \{A_0(1-2\nu)+C_0(4-4\nu)\}\kappa\eta$$
$$+ \sum_{n=1}^{\infty} G_n\frac{\sin(n\pi\eta)}{\beta_n}\Big\{\Big(-2+2\nu+\beta_n\frac{I_0}{I_1}\Big)$$
$$\times \frac{I_0(\beta_n\rho)}{I_1} - \beta_n\rho\frac{I_1(\beta_n\rho)}{I_1}\Big\}$$
$$+ \sum_{s=1}^{\infty} H_s\frac{J_0(\lambda_s\rho)}{\lambda_s}\Big(\gamma_s\coth\gamma_s\frac{\sinh\gamma_s\eta}{\sinh\gamma_s}$$
$$- \gamma_s\eta\frac{\cosh\gamma_s\eta}{\sinh\gamma_s}\Big)$$

$$\frac{uE}{1+\nu}/(q_0a) = -C_0\rho + \sum_{n=1}^{\infty} G_n\frac{\cos(n\pi\eta)}{\beta_n}$$
$$\times\Big\{\Big(-2+2\nu-\beta_n\frac{I_0}{I_1}\Big)\frac{I_1(\beta_n\rho)}{I_1}$$
$$+ \beta_n\rho\frac{I_0(\beta_n\rho)}{I_1}\Big\}$$
$$+ \sum_{s=1}^{\infty} H_s\frac{J_1(\lambda_s\rho)}{\lambda_s}\Big\{(3-4\nu-\gamma_s\coth\gamma_s)$$
$$\times \frac{\cosh\gamma_s\eta}{\sinh\gamma_s} + \gamma_s\eta\frac{\sinh\gamma_s\eta}{\sinh\gamma_s}\Big\} \tag{10}$$

We obtain the following equations from Eq. (10), by using the Fourier expansion and the Fourier-Bessel expansion.

on $\rho = 1$,

$$\sigma_r/q_0 = A_0\nu + C_0(2\nu-1) + \sum_{s=1}^{\infty} H_sP_s$$
$$+ \sum_{n=1}^{\infty}\cos(n\pi\eta)\Big(G_n\Delta_n + \sum_{s=1}^{\infty} H_sQ_{ns}\Big)$$
$$(-1 < \eta < 1)$$

on $\eta = \pm 1$,

$$\frac{uE}{1+\nu}/(q_0a) = \sum_{s=1}^{\infty}\frac{J_1(\lambda_s\rho)}{\lambda_s}\Big(C_0\frac{2}{J_0} + H_s\Omega_s$$
$$+ \sum_{n=1}^{\infty} G_nR_{sn}\Big) \qquad (0 \le \rho < 1) \tag{11}$$

in which, $J_0 = J_0(\lambda_s)$ and

$$\Delta_n = \{2-2\nu+{\beta_n}^2-{\beta_n}^2(I_0/I_1)^2\}/\beta_n$$
$$\Omega_s = (3-4\nu)\coth\gamma_s - \gamma_s\,\mathrm{cosech}^2\,\gamma_s$$
$$P_s = (2-2\nu)J_0/\gamma_s$$
$$Q_{ns} = (-1)^n 4\gamma_s J_0\frac{(1-\nu){\gamma_s}^2+(2-\nu)(n\pi)^2}{\{{\gamma_s}^2+(n\pi)^2\}^2}$$
$$R_{sn} = \frac{(-1)^n 4{\lambda_s}^2}{\beta_n J_0}\cdot\frac{(2-\nu){\beta_n}^2+(1-\nu){\lambda_s}^2}{({\beta_n}^2+{\lambda_s}^2)^2} \tag{12}$$

Substituting Eq.(10) into Eq.(3e) and using Eq.(2), we obtain the following equation:

$$A_0(1-\nu) + C_0(4-2\nu) = 1 \tag{13}$$

Using the Fourier-Bessel expansion, we shall express the displacement function $u(\rho)$ on the loading end in Eq.(3d) by the following formula.

$$u(\rho) = \alpha u_0\sum_{s=1}^{\infty} a_sJ_1(\lambda_s\rho) \qquad (0 \le \rho < 1) \tag{14}$$

Next simultaneous equations are obtained as the results of substitution of Eqs. (1),(11),(13),(14) into Eqs. (3a) and (3d):

$$\left.\begin{aligned} &C_0\frac{2}{J_0} + H_s\Omega_s + \sum_{n=1}^{\infty} G_nR_{sn} \\ &\qquad = \alpha\frac{(1-\nu)p_0/q_0-\nu}{1+\nu}\lambda_sa_s \\ &G_n\Delta_n + \sum_{s=1}^{\infty} H_sQ_{ns} = 0 \\ &C_0 - \frac{1-\nu}{1+\nu}\sum_{s=1}^{\infty} H_sP_s \\ &\qquad = \frac{\nu}{1+\nu} - \frac{1-\nu}{1+\nu}(p_0/q_0) \end{aligned}\right\} \tag{15}$$

The solutions of Eqs.(13) and (15) are A_0, C_0, G_n, and H_s. The number of equations for C_0 and m unknowns G_n and H_s is $(2m+1)$.

Two displacement functions were used in this

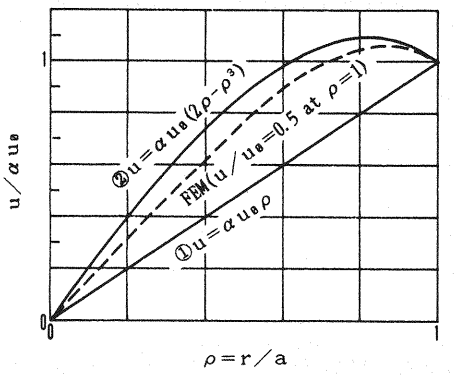

Fig. 2 Forms of radial displacement on the loading end.

paper, which are shown in **Fig. 2** as ① and ②. The coefficients a_s in Eq.(14) for these functions are as follows:

① For the case $u(\rho) = \alpha u_0 \rho$,

$$a_s = \frac{-2}{\lambda_s J_0(\lambda_s)} \tag{16}$$

② For the case $u(\rho) = \alpha u_0 (2\rho - \rho^3)$,

$$a_s = \frac{-2}{\lambda_s J_0(\lambda_s)} \left(1 + \frac{8}{\lambda_s{}^2}\right) \tag{17}$$

When we use $\alpha = 1$, the radial displacement u for case ① coincides with that of the basic solution, which is useful to estimate the accuracy of the numerical results. The broken line in **Fig. 2** indicates the radial displacement on the loading end obtained with the finite element method. This line resembles line ②. The boundary condition of this result with the finite element method was $u = u_0/2$ at $\rho = \eta = 1$. However, the actual distribution of radial displacements on the loading ends in the usual compression tests is unknown.

(3) Numerical method

Numerical computations were carried out with the above analytical solutions. The series summation in Eq. (10) converged very slowly on the boundary lines $\eta = 1$ and $\rho = 1$, but they varied cyclically. Accordingly, series summations were replaced by the mean value of those of each cycle and the computations were continued until these mean values converged to a prescribed accuracy. The error of numerical results thus obtained could be estimated by comparing those with the values of the boundary conditions. The cycle of series depended on the value of ρ and η, but the least common multiple was $n = s = 40$. Hence, the convergence in all points of the cylinder was estimated by $n = s = 40$. However, the computations were terminated at $n = s = 400$, regardless of the convergence. With the exception of point $\rho = \eta = 1$, the results thus obtained were almost the same as those of $n = s = 800$. Numerical results for the analytical solution cannot be obtained at the point $\rho = \eta = 1$, because Eqs.(11) and (14) are not defined at this point. Numerical results agreed with the boundary condition by four digits at the point $\eta = 1$ and $\rho = 0.95$, but a slight error was seen at the point $\rho = 1$ and $\eta = 0.95$. In any case, the point $\rho = \eta = 1$ is an analytically singular point, then the numerical displacement u used at this point was that of a boundary condition in the following chapter. The series summation of σ_z did not oscillate at the point $\rho = \eta = 1$ when $\alpha < 1$, but it continued to increase with the increases of n and s. In this connection, it is commonly known that the value of σ_z at the contact end of a rigid plate with a semi-infinite elastic body is infinite.

An asymptotic expansion equation and an approximate equation were used in the numerical computation to prevent exponential overflow. The numerical computations were carried out with double precision using subroutines SSL II and NUMPAC of FACOM in Kyoto University.

4. NUMERICAL EXAMPLES AND DISCUSSION

Numerical computations of the analytical solutions were carried out for $\nu = 0.20$. Several values of κ, α and p_0/q_0 were selected, and two radial displacement functions on the loading end were used. Some of these numerical results were compared with those obtained with the finite element method using the program EPIC IV[8]. This program is based on the triangular elements with constant strains and stresses in each element where r and z in matrix [B] have been replaced by the average values of those at the three nodal points. The accuracy of this program was verified for the basic solutions mentioned above, and the solution was correct up to the fourth significant digits.

(1) Effects of size ratio and degree of constraint on the radial displacement of the side surface

The distributions of u/u_0 on the side surface shown in **Fig. 3** were computed under the conditions of Eq.(16), and $\kappa = 0.17 - 2.0$, $p_0 = 0.0$, α =0.0 and 0.5. The abscissa indicates the ratio of radial displacement compared to that of the basic solution. When $\kappa \geq 1$, it is seen that the radial displacement of the side surface in the mid-

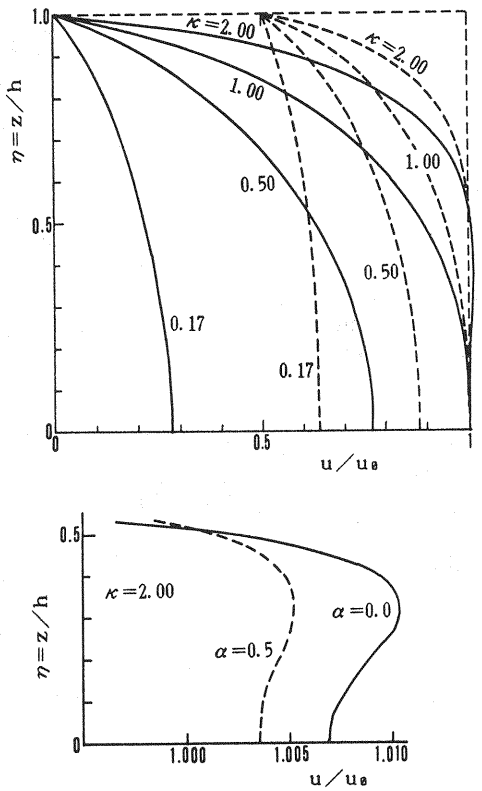

Fig. 3 Distribution of relative radial displacement on the side surface. Lower graph shows details of the upper one. (ν =0.2, p_0=0.0)

dle part of the height was slightly larger than that of the basic solution. In particular, a large bulge appeared when the degree of constraint was large. Details of this phenomenon are shown in the lower graph of **Fig. 3**. On the other hand, when $\kappa \leq 0.5$, radial displacements at all places on the side surface were smaller than those of the basic solution, and a small bulge appeared for the larger degree of constraint.

As illustrated in the lower graph of **Fig. 3**, the side bulge for $\kappa = 2.0$ did not increase monotonously from the loading end to the middle part of the height. The bulge was largest at a height near $\eta = 1/3$ and decreased toward the center. Such double bulges have been reported as the results of experiments using aluminum cylinders of κ =2.50 and 2.75. The cylinders in these experiments were compressed uni-axially to the plastic limit and elasto-plastic analyses were also carried out with the finite element method[9].

(2) Axial displacement of the loading end

When free radial displacement on the loading end was partially constrained, the axial displacement of the loading end ($w_{\eta=1}$) became smaller than that of the basic solution (w_0). The values of $w_{\eta=1}/w_0$ for $p_0 = 0$ are shown in the 2nd and 3rd columns of **Table 1.** The axial displacement of the loading end decreased when the degree of constraint of the radial displacement on the loading end increased.

Table 1 Relative axial displacement of loading end ($w_{\eta=1}/w_0$)

	Analytical		FEM	
	α		α	
κ	0.0	0.5	0.5 (η=1)	0.5 (η=0)
2.00	0.9891	0.9946	0.9980	0.9943
1.00	0.9781	0.9899	0.9922	0.9885
0.50	0.9555	0.9778	0.9805	0.9794
0.17	0.9197	0.9588	0.9594	0.9563

ν =0.2, p_e=0.0

When the radial displacement on the loading end is constrained, the axial displacement and the average load intensity on this end are initially unknown. Hence, in the finite element method, it is impossible to give the axial displacement on the loading end as a boundary condition corresponding to the prescribed average load intensity. If the value of w_0 is used as a boundary condition, the resultant of σ_z computed from nodal reactions on the loading end will disagree with that of the basic solution. Now, we will introduce a modification coefficient k defined in the following equation:

$$k = \int_0^a \sigma_z 2\pi r dr / q_0 \pi a^2 \qquad (18)$$

The value of $1/k$ coincides with that of the displacement ratio $w_{\eta=1}/w_0$. Such k values can also be obtained from nodal reactions on the plane $\eta = 0$, but these coefficients usually disagree. The displacement ratios thus obtained are shown in the 4th and 5th columns of **Table 1**. The equation for obtaining the value of σ_z on the nodal points of the loading end in the finite element method will be described in section (7) of this chapter.

(3) Distribution of axial stress on the loading end

The distribution of σ_z on the loading end is shown in **Fig. 4**. The analytical solution of σ_z at the point $\eta = \rho = 1$ cannot be obtained for the above mentioned reason. The numerical results of the finite element method at this point are also beyond the scale of **Fig. 4**. Therefore, the graph was omitted near this point. Contours in this part shown later were omitted for the same reason. **Figs. 4(a),(b)** indicate results obtained

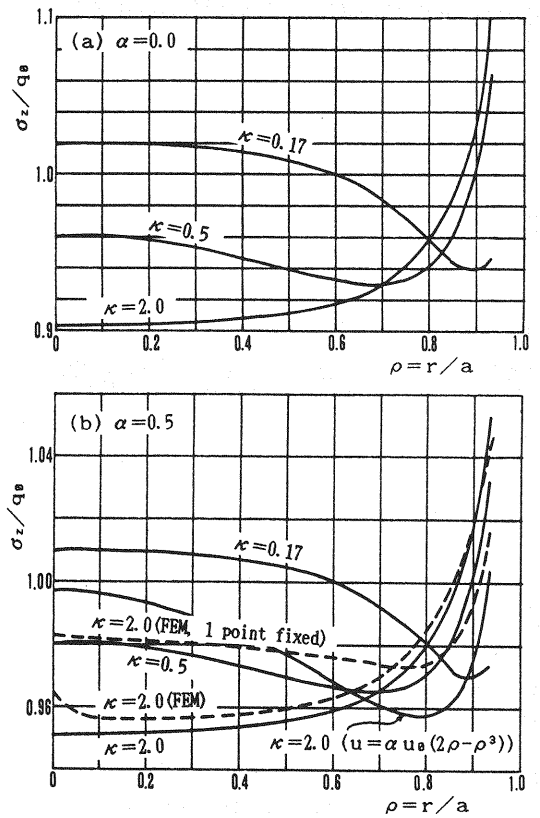

Fig. 4 Distribution of σ_z on the loading end. ($\nu = 0.2, p_0 = 0.0$)

under the conditions of $\alpha = 0$ and 0.5, respectively. The non-uniformity of σ_z on the loading end appeared more strongly when the degree of constraint of radial displacement on the loading end was larger. The distribution of σ_z for $\kappa = 1.0$ was almost the same as that for $\kappa = 2.0$. Accordingly, the results for $\kappa = 1.0$ were omitted. All curves in **Fig. 4(a)** and the three curves in **Fig. 4(b)** indicate results for Eq.(16). It can be seen in these results that the minimum value of σ_z appeared at the point $\rho = 0$ when $\kappa = 2.0$, but this appeared at a point near $\rho = 0.7$ when $\kappa = 0.5$. On the other hand, the curves for the disc-shaped cylinder of $\kappa = 0.17$ were different. The value of σ_z at $\rho = 0$ was larger than q_0, and the minimum appeared at a point near $\rho = 0.85$. Examples of the results obtained with the finite element method are shown by broken lines in **Fig. 4(b)**. Although the results obtained with the finite elements method for the basic solution were very accurate, those for the constraint condition contained error.

One of the broken lines in **Fig. 4(b)** is the result for Eq.(16) while the other is for the boundary condition that the radial displacement only on the perimeter $\rho = \eta = 1$ was given. As shown in **Fig. 2**, the distribution of u on the loading end for Eq.(17) was similar to that from the finite element method when radial displacement was given only on the perimeter. However, less similarity between them was shown in the distribution of σ_z. The boundary condition for the broken line in **Fig. 2** coincides with that for the broken line marked '1 point fixed' in **Fig. 4(b)**.

(4) Distribution of stresses and strains

In the following, the stresses and strains are shown in percentage relative to q_0; those for the basic solutions will be shown by broken lines. The contours of the stresses and strains in a quarter of the cylinder of $\kappa = 2.0$, $\alpha = 0.5$ and $p_0 = 0.0$ are shown in **Fig. 5**. These contours were drawn from the values at 496 grid points. The $\overline{\sigma}$ shown in **Fig. 5(a)** is the equivalent stress and was computed by the following equation[10]:

$$\overline{\sigma} = \sqrt{\{(\sigma_1 - \sigma_2)^2 + (\sigma_2 - \sigma_3)^2 + (\sigma_3 - \sigma_1)^2\}/2} \tag{19}$$

in which, $\sigma_1, \sigma_2, \sigma_3$ are the principal stresses. A relation between $\overline{\sigma}$ and the octahedral shearing stress τ_{oct} has been proposed[11] as $\tau_{oct} = (\sqrt{2}/3)\overline{\sigma}$, and a relation between $\overline{\sigma}$ and the octahedral shearing strain γ_{oct} has been proposed[12] as $E\gamma_{oct} = (2\sqrt{2}/3)(1+\nu)\overline{\sigma}$. The relation between shearing strain strength S and γ_{oct} has also been proposed[13] as $S = 0.612\gamma_{oct}$. These equations imply that the shapes of contours of τ_{oct}, γ_{oct} and S perfectly coincide with that of $\overline{\sigma}$.

It can be seen from **Figs. 5(a),(b)** that the absolute maxima of $\overline{\sigma}$ and τ_{max} took place at the point $\rho = \eta = 1$, and the maxima on the line $\rho = 0$ took place at about $\eta = 0.46$. Those maxima at both points were greater than the values of the basic solution and the line between them formed a ridge. The minima of $\overline{\sigma}$ and τ_{max} took place at the center of the loading end. The distribution of $E\epsilon_1$ shown in **Fig. 5(c)** was similar to these, but the maximum on the line $\rho = 0$ took place at about $\eta = 0.33$. It is interesting that the shape of the ridges of $\overline{\sigma}$, τ_{max} and $E\epsilon_1$ resembles the conical fracture frequently observed in the usual compression tests.

The contour of $E\epsilon_t$ shown in **Fig. 5(d)** was different from the other three. The value of $E\epsilon_t$ at the relative height $\eta > 0.5$ was smaller than that of the basic solution, but was larger at $\eta < 0.5$. The maximum of $E\epsilon_t$ on the line $\rho = 0$ took place at about $\eta = 0.33$. The maxima of $E\epsilon_t$ on the side surface was seen also at about $\eta = 0.33$. This point corresponded to the position of the maximum bulge shown in **Fig. 3**.

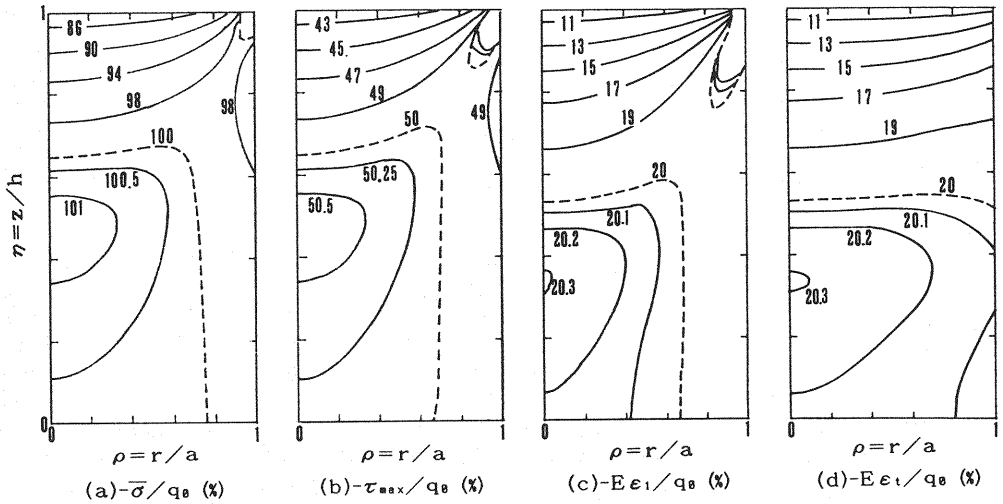

Fig. 5 Contours of stresses and strains in a quarter of a cylinder. Broken lines represent the values of Eq.(1). ($\nu = 0.2$, $\kappa = 2.0$, $\alpha = 0.5$, $p_0 = 0.0$)

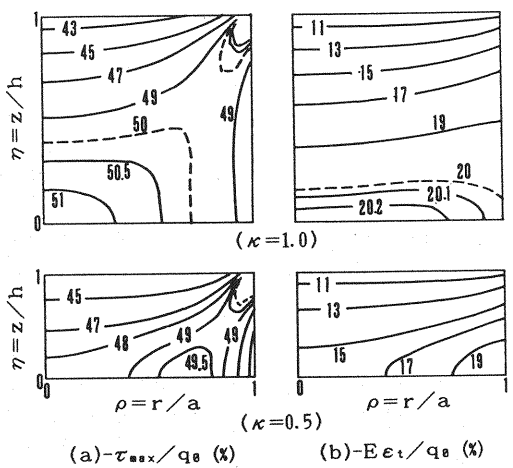

Fig. 6 Effect of the ratio of height to diameter on the τ_{max} and $E\epsilon_t$. Broken lines represent the values of Eq.(1). ($\nu = 0.2$, $\alpha = 0.5$, $p_0 = 0.0$)

(5) Effects of size ratio

Numerical computations for the cylinders of $\kappa = 1.0$ and 0.5 were carried out under the same conditions as in **Fig. 5**. Those results are shown in **Fig. 6**. The figure of τ_{max} for $\kappa = 1.0$ generally resembled in shape the upper half of **Fig.5(b)**. However, the position of the contour on the middle part of the height was slightly different from that of the relative height about $\eta = 0.5$ for $\kappa = 2.0$. In contrast, the position of the contours for $\kappa = 0.5$ were different from those for $\kappa = 2.0$ and 1.0. There appeared only one contour for the basic solution and, except near the point $\rho = \eta = 1$, τ_{max} was smaller than that of the basic solution. Similar results were seen in $\overline{\sigma}$ and $E\epsilon_1$, but the figures were omitted. Analogous phenomena were seen in the contour of $E\epsilon_t$. However, the value of $E\epsilon_t$ in all parts of the cylinder with $\kappa = 0.5$ was smaller than that of the basic solution (0.200). This fact is related to the side bulge shown in **Fig. 3**. Namely, when the radial displacement on the loading end was constrained, the radial displacement on the side surface of the cylinder of $\kappa \geq 1$ was somewhat larger than the basic solution, but such phenomenon did not appear in the cylinder of $\kappa \leq 0.5$. The phenomena were seen more evidently when $\kappa = 0.17$ than when $\kappa = 0.5$.

Stresses and strains in some portions of the cylinder of $\kappa \geq 1$ were larger than those of the basic solution, but in another part they were smaller. However, stresses and strains for almost all parts of the cylinder with $\kappa \leq 0.5$ were smaller than those of the basic solution. Accordingly, if we use stresses and strains as fracture criteria, the effect of size ratio on the strength will be ambiguous for the cylinder of $\kappa \geq 1$, but will be distinct for the cylinder of $\kappa \leq 0.5$. Experimental results[14),15)] have supported these discussions. In other words, when the size ratio κ was smaller than 0.5, the strength of the cylinder increased evidently with the decrease of κ.

(6) Effects of degree of constraint and confining pressure

The contour of τ_{max} under the conditions of $p_0 = 0.0$ and $\alpha = 0.0$ is shown in **Fig. 7(a)**. This is an example showing the effect of degree of constraint on the loading end. The position of the contour for the basic solution coincides with that for $p_0 = 0.0$ and $\alpha = 0.5$ shown in **Fig. 5(b)**. The

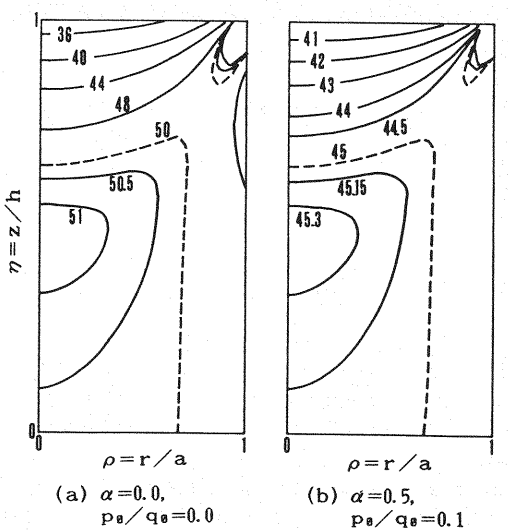

Fig. 7 Effects of degree of constraint and confining pressure on the $-\tau_{max}/q_0(\%)$. Broken lines represent the values of Eq.(1). ($\nu = 0.2, \kappa = 2.0$)

position of contours of another set of stresses and strains indicates the same results, but the differences in stresses and strains between the condition for $\alpha = 0.0$ and those of the basic solution were twice that for the case for $\alpha = 0.5$. It can be seen from Eq.(1), that $u_0 = 0$ and $\tau_{rz} = 0$ are satisfied on the loading end when the following equation is satisfied because, regardless of the value of α, the equation $u = 0$ in all parts of the cylinder is satisfied.

$$p_0/q_0 = \nu/(1-\nu) \tag{20}$$

Fig. 7(b) is an example of the contour of τ_{max} under the condition of

$$p_0/q_0 < \nu/(1-\nu) \tag{21}$$

The position of the contour of the basic solution in this figure was also the same as that of **Fig. 5(b)** and **Fig. 7(a)**. The same conclusions were obtained for other values of α and p_0/q_0 satisfying Eq.(21).

As a result, it can be concluded that all contours of stresses and strains in any cylinder subjected to a load satisfying Eq.(21) will be similar despite the value of α and p_0/q_0. Furthermore, the shape of the contours will coincide with those of the cylinder whose radial displacement on the loading end is perfectly constrained. However, the reasons for these phenomena are still unknown. When the radial displacement on the loading end was given by Eq.(17), the contours were very different from those shown in the above figures, but these are omitted in this paper.

(7) Modification and accuracy of the finite element results

The mesh used in the finite element method is chosen referring to a reported example[9]. In the cylinder of $\kappa = 2.0$, the 300 squares with 336 nodes were divided into 600 right triangles by diagonals starting from the bottom left corner of each square. The given boundary conditions on the loading end were the axial displacement w_0 and radial displacement on the loading end. When the stresses and strains thus obtained were divided by the value k computed from Eq.(18), the boundary conditions of these solutions will coincide with those of the analytical solutions. Now, the relation between the nodal reaction F_z and the normal stress σ_z of Eq.(18) of the axi-symmetric problem differs from that of the two-dimensional problem. The relation between load intensity q_0 of a uniform load and nodal loads P_i and P_k has been shown by the following equations[17], which were verified by the basic solutions:

$$\left.\begin{aligned} P_i &= \pi(r_k + 2r_i)(r_k - r_i)q_0/3 \\ P_k &= \pi(2r_k + r_i)(r_k - r_i)q_0/3 \end{aligned}\right\} \tag{22}$$

The nodal load P is equivalent to the nodal reaction F_z and q_0 is also equivalent to σ_z. Therefore, one has the following equation:

$$\sigma_z = F_z q_0/P \tag{23}$$

Stresses in the small interval were regarded as uniform, and the k value was computed by substituting σ_z of Eq.(23) into Eq.(18). The computations of the finite element method were carried out by HITAC of Tottori University, and the Newton-Cotes 9 points rule was used for the integration of Eq.(18).

As shown in **Table 1**, the value of $1/k$ computed on the lines $\eta = 1$ and $\eta = 0$ disagreed slightly. Stresses and strains modified from the same finite element results using these k values also slightly disagreed. As a result, when the gradients of stresses and strains were small, the position of the contour having the same value was greatly different. An example of such phenomenon is shown in **Fig. 8**. **Fig. 8(a)** indicates the contour of τ_{max} modified by the k value on the line $\eta = 1$ while **Fig. 8(b)** indicates that modified by the k value on the line $\eta = 0$. Even though the relative error of both $1/k$ values shown in **Table 1** was 0.8%, the positions of the basic solution illustrated in **Figs. 8(a),(b)** were very different. Among these figures, **Fig. 8(b)** almost agreed with the analytical results shown in **Fig. 5(b)**. **Fig.8(b)** illustrated the modified results using

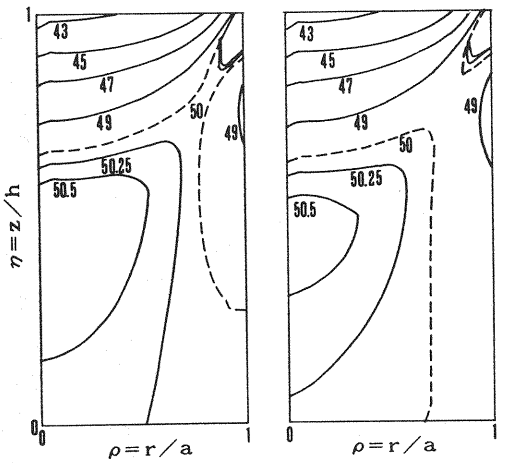

(a) 1/k=0.9980 in η=1 (b) 1/k=0.9943 in η=0

Fig. 8 Contours of the $-\tau_{max}/q_0$(%) obtained with the finite element method. Results obtained with the finite element method were modified by the resultant of axial reaction on (a) the loading end and (b) the middle height of cylinder. Broken lines represent the values of Eq.(1). ($\nu = 0.2$, $\kappa = 2.0$, $\alpha = 0.5$, $p_0 = 0.0$)

nodal reactions on the line $\eta = 0$. The line $\eta = 0$ lies away from the loading end of $\eta = 1$. Hence, according to Saint-Venant's principle, the distribution of σ_z on the line $\eta = 0$ will approach uniform. Consequently, the degree of agreement of Eqs.(22) and (23) on the line $\eta = 0$ was higher than that on the line $\eta = 1$. The computations by the finite element method were carried out for finer meshes than those mentioned above. The region was divided into the 800 squares with 861 nodes, and each square was divided into two right triangles by a diagonal starting from the bottom left corner of each square. The accuracy of results for these elements was higher than those shown above. The value of $1/k$ on $\eta = 0$ was 0.9945, which was very close to the analytical value 0.9946. Contours near the loading end were also close to those of the analytical solution.

Contours of stresses and strains in the isotropic homogeneous elastic body have no singular points in nature. Accordingly, the tangent of these contours on the line $\rho = 0$ should be parallel to the abscissa, but **Fig. 8** was inconsistent with this prediction. The **[B]** matrix in the finite element method for the axi-symmetric problem has a characteristic form, so this is considered one of the reasons for such inconsistency. Even with densely divided elements, the results of the finite element method were still incondistent. However, the contours in **Figs. 5-7** obtained from the analytical results did not indicate any inconsistency.

The computations under the same boundary conditions mentioned above were carried out by the finite element method for the right triangle elements made by a diagonal of squares starting from the bottom right corner. However, the degree of accuracy of these results was lower than those described above.

5. SUMMARY

The derivation of analytical elastic solutions and the numerical method about them for isotropic homogeneous circular cylinders subjected to unconfined or confined axi-symmetric loads through a rigid platen were described. It was assumed that radial displacement on the loading end was partly or perfectly constrained. Numerical computations were carried out under several cases of size ratio, degree of constraint, pressure ratio and radial displacement form. The basic solutions of these problems are those for the frictionless condition on the loading end. Surface displacements, reaction distribution on the loading end and contours of stresses and strains under the constraint condition were compared with those of the basic solutions. Accuracy of the results by the finite element method was also discussed. Results obtained are summarized as follows.

(1) Elastic solutions for the cylinder shown in **Fig.1(b)** were obtained using Love's stress function. Boundary conditions and equilibrium equations are shown by Eq.(3). If the values of A_0, C_0, and m sets of G_n and H_s are obtained by solving simultaneous Eqs.(15), stresses and displacements at any point of the cylinder can be calculated by Eq.(10). Distributions of radial displacement on the loading end were given by Eq.(14) using the Fourier-Bessel expansion; the coefficients for this equation were calculated by Eqs.(16),(17).

(2) When radial displacement on the loading end was constrained, the radial displacement at the middle part of the side of the cylinder with the size ratio $\kappa = h/a \geq 1.0$ were greater than that of the basic solution. A large side end bulge appeared when a great value of degree of constraint on the loading end was given. The maximum side end bulge in the cylinder with size ratio $\kappa = 2.0$ appeared at the relative height of about $\eta = z/h = 1/3$. However, when κ was less than 0.5, the radial displacement on all parts of the side end was smaller than that of the basic solution. Moreover, the radial displacement for the cylinder of $\kappa \leq 0.5$ was small when the degree of

constraint was large.
(3) The minimum value of σ_z on the loading end in the cylinder of $\kappa \geq 1.0$ appeared at the relative radius $\rho = r/a = 0$, but for the cylinder of $\kappa = 0.5$, the minimum appeared at near $\rho = 0.7$. When a disc-shaped cylinder of $\kappa = 0.17$ was used, the minimum σ_z on the loading end appeared near $\rho = 0.85$, and the value of σ_z at $\rho = 0$ was larger than the average load intensity q_0.
(4) When the radial displacement on the loading end of a cylinder of $\kappa = 2.0$ was constrained, the ridges of the contours of $\overline{\sigma}$, τ_{max} and ϵ_1 formed a conical shape. The value of ϵ_t near the loading end was smaller than that of the basic solution, but its value at the middle part of the cylinder was larger than that of the basic solution. In addition, the maximum ϵ_t appeared at the inner part of the cylinder.
(5) Distributions of stresses and strains in the cylinder with size ratio $\kappa = 1.0$ were analogous to those near the loading end of $\kappa = 2.0$. Stresses and strains in all part of the cylinder with size ratio $\kappa \leq 0.5$ were smaller than those of the basic solution
(6) When the radial displacement on $\eta = 1$ was assumed to be proportional to the radial distance from the axis, the distributions of stresses and displacements in the cylinder were similar to those of the cylinder with a perfectly constrained radial displacement on the loading end. This phenomenon was independent of the degree of constraint and pressure ratio p_0/q_0.
(7) Boundary conditions used in the analytical solutions shown in this paper cannot be applied to the finite element method because the relation between load and axial displacement of the loading end is initially unknown. Accordingly, modifications of the finite element results were required. However, positions of contour lines of stresses and strains thus obtained greatly disagreed with those of the analytical solution where gradients of stresses and strains were small. The accuracy of the finite element method was better with a finer mesh, but inaccuracy of the results near the axis still remained.

The boundary conditions shown by Eq.3(c) indicate that the cylinder is in contact with rigid platens, but the Young's modulus of the platen used in the usual compression tests has finite value. Therefore, Eq.3(c) does not perfectly coincide with the boundary condition of the usual compression test.

The author would like to thank Professor Okumura of Kitami Technological College for his kind advice on this manuscript.

REFERENCES

1) Filon, L.N.G.: On the elastic equilibrium of circular cylinders under certain practical systems of load, *Phil.Trans.Royal Soc.*, Vol.198, pp.147-223, 1902.
2) Kimura, J.: On the stress distribution in the cylinder under compression test, *J.JSCE*, Vol.17, pp.713-731+Appendix, 1931. (in Japanese)
3) Saitō, H.: The axially symmetrical deformation of a short cylinder, *Trans.JSME*, Vol.18,No.68, pp.21-28, 1952, Vol.20,No.91, pp.185-190, 1954. (in Japanese)
4) Yamaguchi, H.: *Mechanics of Elasto-Plasticity*, Morikita Shuppan, Tokyo, pp.168-172, 1975. (in Japanese)
5) Ogaki, Y. and Nakajima, N.: Stress analysis of a circular cylinder of finite length subjected to loads symmetrical to middle plane and to axis of revolution, *Sci.Eng.Review of Doshisha Univ.*, Vol.23,No.4, pp.195-205, 1983. (in Japanese)
6) Murakami, T.: *Mechanics of Elasticity*, Yokendo, Tokyo, pp.5-8, 43-44, 1989. (in Japanese)
7) Love, A.E.H.: *A Treatise on the Mathematical Theory of Elasticity*, 4th ed., Dover Publications, pp.274-276, 1944.
8) Yamada, Y. and Yokouchi, Y.: *Elasto-Plastic Analytical Programming by the Finite Element Method*, Baifukan, Tokyo, 1981. (in Japanese)
9) Nagamatsu, A. Murota, T. and Jimma, T.: On the non-uniform deformation of material in axially symmetric compression caused by friction. Part 1 and Part 2, *Trans.JSME*(I), Vol.36,No.288, pp.1276-1284, 1285-1296, 1970. (in Japanese)
10) Crandall, S.H. and Dahl, N.C. eds.: *An Introduction to the Mechanics of Solids*, Translated by Okumura, A. and Hayashi, T., Koronasha, Tokyo, pp.227-233, 1967. (in Japanese)
11) Okada, K. and Muguruma, H. eds.: *Concrete Handbook*, Asakurashoten, Tokyo, pp.427-430, 1981. (in Japanese)
12) Kajita, T., Akimoto, M. and Kawamoto, T.: On the effect of end restraint of cylindrical brittle specimen on its states of deformation and compressive strength, *Proc.JSCE*, No.166, pp.27-38, 1969. (in Japanese)
13) Hata, T.: Deformation and failure of concrete under combined compressive stresses, *Trans.JSCE*, No.143, pp.22-27, 1967. (in Japanese)
14) Gonnerman, H.F.: Effect of size and shape of test specimen on compressive strength of concrete, *Proc.ASTM*, Part II, pp.237-255, 1925.
15) Okushima, M. and Kosaka, Y.: Effect of frictional condition of loading face on compressive strength of concrete specimen, 18th *Review General Meeting, Japanese Cement Eng. Assoc.*, pp.159-164, 1966.
16) *op. cit.* 11), pp. 376-380
17) Miyoshi, T. and Shiratori, M.: *Practice in the Finite Element Method*, Saiensusha, Tokyo, pp.93, 174-175, 1986. (in Japanese)